A chiral inverse Faraday effect mediated by an inversely designed plasmonic antenna

Ye Mou, Xingyu Yang, Bruno Gallas, Mathieu Mivelle

A Chiral Inverse Faraday Effect Mediated by an Inversely Designed Plasmonic Antenna

Ye Mou, Xingyu Yang, Bruno Gallas, and Mathieu Mivelle*

Sorbonne Université, CNRS, Institut des NanoSciences de Paris, INSP, F-75005 Paris, France

*Corresponding author: mathieu.mivelle@sorbonne-universite.fr

Abstract

The inverse Faraday effect is a magneto-optical process allowing the magnetization of matter by an optical excitation carrying a non-zero spin of light. This phenomenon was considered until now as symmetric; right or left circular polarizations generate magnetic fields oriented in the direction of light propagation or in the counter-propagating direction. Here, we demonstrate that by manipulating the spin density of light in a plasmonic nanostructure, we generate a chiral inverse Faraday effect, creating a strong magnetic field of 500 mT only for one helicity of the light, the opposite helicity producing this effect only for the mirror structure. This new optical concept opens the way to the generation of magnetic fields with unpolarized light, finding application in the ultrafast manipulation of magnetic domains and processes, such as spin precession, spin currents and waves, magnetic skyrmion or magnetic circular dichroism, with direct applications in data storage and data processing technologies.

Keywords: plasmonic nanoantenna, inverse Faraday effect, inverse design, light−matter interactions, chirality

1. Introduction

The inverse Faraday effect (IFE) is a magneto-optical process enabling the magnetization of matter by optical excitation only[1-3] (Figure 1). This magnetization is made possible by the action of non-linear optical forces on the matter's electrons.[4-7] In particular, in a metal, the free electrons subject to these non-linear forces are set in a drift motion at the origin of the IFE. If we consider these electrons as free-moving charges, the expression of these drift currents ($\mathbf{J_d}$) can be described using the plasma community's formalism[8, 9] developed. In this case, R. Hertel demonstrated that in metal, $\mathbf{J_d}$ is written as:[7, 10]

$$\mathbf{J_d} = \frac{1}{2en}\mathrm{Re}\left(\left(-\frac{\nabla\cdot(\sigma_\omega \mathbf{E})}{i\omega}\right)\cdot(\sigma_\omega \mathbf{E})^*\right) \qquad (1)$$

With e the charge of the electron (e < 0), n the charge density at rest, σ_ω the dynamic conductivity of the metal, and **E** the optical electric field.

These drift currents are, therefore, a function of the optical electric field and its divergence. Because of their ability to manipulate fields and field gradients, nanophotonics and nanoplasmonics are then particularly well suited to generate a strong IFE and thus create, through the Biot and Savart equation (Equation (2)), strong stationary magnetic fields (**B**).[11-16]

$$\mathbf{B} = \frac{\mu_0}{4\pi}\iiint \frac{\mathbf{J_d}\times\mathbf{r}}{|\mathbf{r}|^3}\,dV \qquad (2)$$

Where μ_0 is the vacuum magnetic permeability, dV is the volume element and **r** is the vector from dV to the observation point.

Moreover, a plasmonic IFE will confine the created **B**-field to sub-wavelength scales due to its nanometric scales.[11, 16] Finally, the generation of the **B**-field by IFE is due to light-matter interactions; therefore, by using ultra-short optical pulses, nanoplasmonics is today the only

technique allowing the creation of intense, confined, and ultra-fast magnetic field pulses.[14, 16, 17]. These unique properties have applications in many fields of magnetic research and technology.[18] Indeed, since the pioneering work of Beaurepaire *et al*,[19] researchers have been looking for ways to manipulate and study magnetization at very short time and spatial scales,[20-24] mainly through the use of femtosecond lasers, intending to control and accelerate current data storage technologies. Unfortunately, the physical processes involved in this type of interaction are still poorly understood. Likewise, the transient processes of magnetic interactions, such as spin precession, spin-orbit coupling, and exchange interactions, have their roots in the femtosecond time scale.[25] The ability to probe and address these different processes and their transient mechanisms using ultrashort pulses of magnetic fields would benefit countless research activities in magnetism: from Zeeman splitting,[26] magnetic trappings,[27] magnetic skyrmions,[28] magneto-plasmonics,[29] ultrafast magnetic modulations,[30] and magnetic circular dichroism[31] to spin control,[32] spin precession,[33] spin currents,[34] and spin waves.[35]

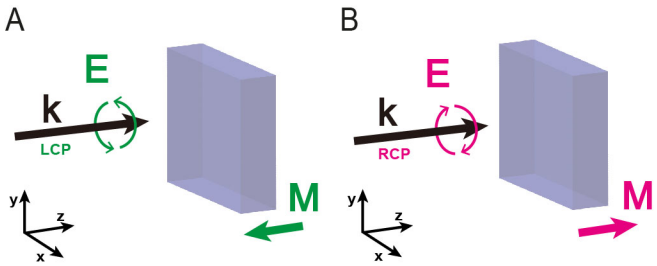

Figure 1: Principle of the inverse Faraday effect. A circularly polarized electromagnetic wave magnetizes a material. This magnetization is oriented A) against the direction of the wave propagation when the light is left circularly polarized and B) in the direction of the light propagation when it is right circularly polarized.

The IFE is a symmetrical process, i.e., the magnetization of matter by a right circular polarized wave will be opposite to a left circular polarized wave. In particular, the magnetic

field created for a right circular polarization will be oriented in the propagation direction of the light, and that of a left circular polarization will be oriented in a counter-propagative way (Figure 1). Although, by analogy with what has been demonstrated in the past in the chiral interactions between light and matter, it is known that a chiral nanostructure interacts differently with right or left circularly polarized light.[36] In these studies, this translates, for instance, into a different distribution of the local chirality density and/or measurements of far field circular dichroism on these chiral structures.

Here, we demonstrate the generation of a chiral IFE through the manipulation of light at the nanoscale and, in particular, via the local manipulation of the spin density (characterizing the degree of circular polarization of a wave). Using an inverse design algorithm, we have generated a plasmonic nanostructure that creates a non-zero **B**-field for a single helicity of light. Moreover, we show that the mirror image of the optimized plasmonic nanostructure generates a non-zero **B**-field oriented in the opposite direction and only for the other helicity of light. Also, under the illumination conditions used here, the amplitude of the created **B**-field is estimated to be 0.5 T, making it one of the strongest generated by a plasmonic nanostructure.[11, 12, 14, 16] Finally, this chiral IFE results from the photonic nanostructures' ability to manipulate light in the near field. Indeed, we demonstrate that this effect is due to generating a spin-density hot spot within this nanostructure for a single excitation polarization of light. These results are particularly important since they imply that this approach allows optically generating, even with unpolarized incoherent light, magnetic fields that are intense, ultrafast, nanoscale, and always oriented in the same direction. Thus, allowing for manipulation, at very short time and space scales, of many magnetic processes.

2. Results and discussions

Specifically, we have optimized, using a genetic algorithm (GA),[37-39] a plasmonic nanostructure made in a thin gold layer of 30 nm thickness deposited on a glass substrate (Figure 2). This nanostructure is based on a 2D matrix of 10x10 elements matrix, each element consisting of metal or air with a size of 28 nm, constituting a total structure size of 280x280 nm^2. These dimensions are chosen to enable the experimental fabrication of this structure by lithography techniques, for instance. For the same reasons and to avoid the non-physical effects that a numerical approach can generate locally, the corners of the nanostructure are smoothed (Figure S1). The excitation of the structure is done by a circularly polarized plane wave, with a wavelength of 800 nm, launched from the substrate side and an energy density of 5.3 mJ/cm^2 (see supporting information for the full simulation parameters). This excitation power is chosen to be below the threshold of what the material can withstand.[40, 41] Each generation of the GA optimization is composed of 200 structures. For each structure, two simulations are performed, one with a right and another with a left circular polarization. The optical response of each structure is calculated by a Finite Difference Time Domain method (see supporting information), and the associated electric field is then used to calculate the drift currents according to the non-linear Equation (1), in the center part of the structure (see supporting information). Hence, Biot and Savart's law (Equation (2)) estimates the field **B** generated under these two excitation conditions at the center of the nanostructure in X, Y and Z (symbolized by the green star in Figure 2) from those calculated drift currents. Note that only the central volume of 1 nm mesh (140x140x32 nm^3, see supporting information) is considered to integrate the drift currents allowing the calculation of the **B** field via Equation (2). We then choose to maximize the difference $\mathbf{B_z}_{\text{-RCP}}$-abs($\mathbf{B_z}_{\text{-LCP}}$) as a GA optimization function, with $\mathbf{B_z}_{\text{-RCP}}$ and $\mathbf{B_z}_{\text{-LCP}}$ the **B**-fields oriented along Z created by a right or left circular polarization, respectively. The evolution from a

generation N to N+1, N being the number of the generation, is then done by keeping the 200 best structures of the generations 1 to N. The breeding of these 200 structures produces half of the structures of the generation N+1, the other half being constituted of mutated structures with a mutation rate of 10%.

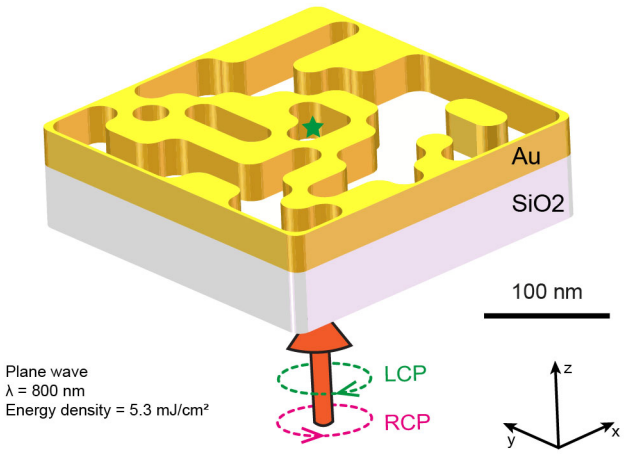

Figure 2: Optimized structure and excitation conditions. Example of a GA-optimized structure, realized in a 30 nm thick gold layer, for excitation by a right- or left-circular polarized plane wave at the wavelength of 800 nm and for an excitation energy density of 5.3 mJ/cm^2. The field **B** generated under the two excitation conditions is evaluated at the center of the gold nanostructure in X, Y and Z (symbolized by the green star)

These optical and selection characteristics give an optimized structure after 76 generations (Figure 2,3A and S2). From the optical response of this optimized structure (Figure S3) and via Equation (1), the associated drift currents are calculated inside the metal (Figure S4). Using Biot and Savart's law, we calculate and show in Figure 3B and C the Z-oriented stationary magnetic field distribution in an XY plane at the Z-center of the optimized structure for left and right circular polarization, respectively. As can be seen, only the right circular polarization generates an intense **B**-field of 0.5 T, oriented in the direction of light propagation (along the positive Z), with an abs($\mathbf{B}_{RCP}/\mathbf{B}_{LCP}$) ratio of 11. Also, using the

plasmonic mirror structure to the optimized one (Figure 3D), we observe that under the same excitation conditions but for a left circular polarization, a **B**-field of the same intensity is generated but oriented in a counter propagative way to the incident light (along the negative Z) and for a left circular polarization. This is the first time a chiral IFE has been observed, moreover with this intensity and at the nanoscale.

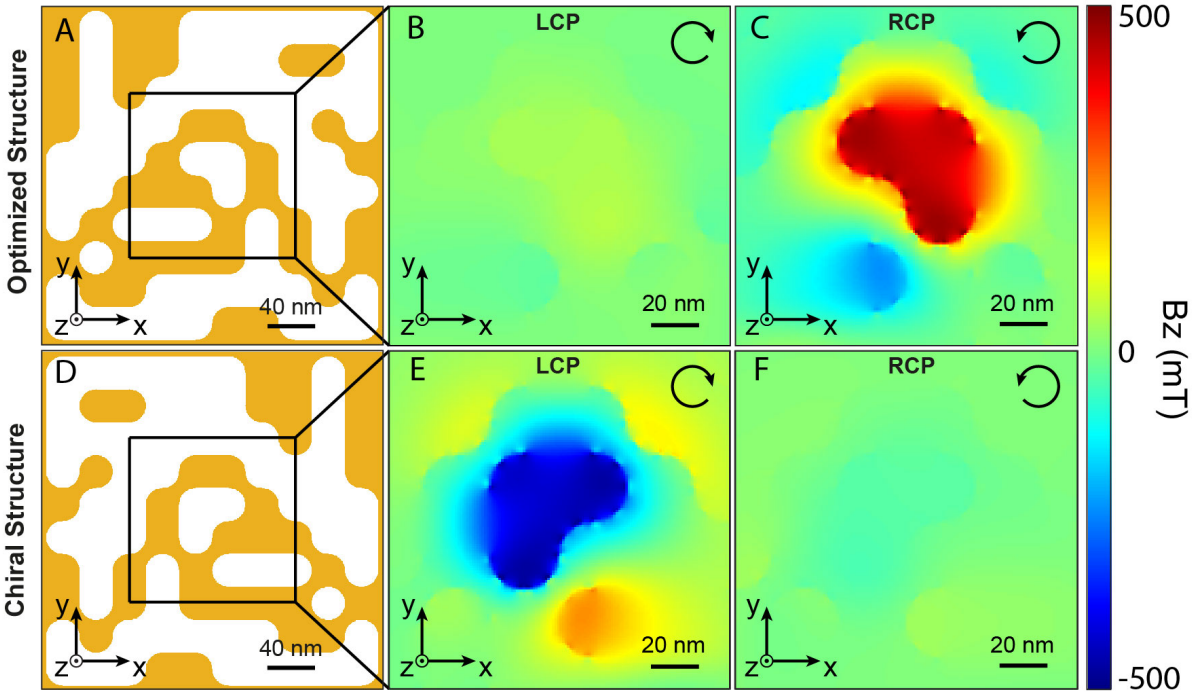

Figure 3: Magnetic response of the optimized plasmonic nanostructure. A) Schematic, in an XY plane, of the GA-optimized structure. B) and C) Spatial distribution of the magnetic field oriented along Z and generated in the Z-center of the structure shown in A) for the left and right circular polarizations of excitation, respectively. D) Schematic, in an XY plane, of the mirror structure displayed in A). E) and F) Spatial distributions of the **B**-field oriented along Z and generated in the Z-center of the mirror structure shown in D) for the left and right circular polarizations of excitation, respectively. See Figure S5 for other **B**-field components and Figure S6 and S7 for its full amplitude in 2D and 3D. The black arrows indicate the incoming polarizations.

The observation of this new physical effect is due to the ability of optical nanostructures to manipulate light and its characteristics in the near field. Indeed, it is known that the manipulation of electromagnetic fields in the near field allows, for instance, to control of local densities of states,[42-44] radiation patterns,[45] chirality densities,[46, 47] or even some nonlinear effects.[48] However, from Equation (1), we can see that a necessary condition must be met to generate drift currents at the origin of the IFE. The light incident on the metal must carry a certain degree of ellipticity so that the product **E.E*** is not zero. In particular, we can see that a right circular or elliptical polarization will generate a stationary magnetic field oriented in the same direction as the propagation of the light. In contrast, a left circular polarization will create it opposite to the propagation direction (Figure 1).[12, 14] Also, a linear polarization will not generate a drift current and, therefore, no magnetic field. Here, we use the unique properties of plasmonic nanostructures to manipulate the spin densities of light locally, or in other words, the local helicity of light to generate a chiral IFE . The equation describing the electric spin density of light is:

$$\mathbf{s} = \frac{1}{|\mathbf{E}_0|^2}\,\mathrm{Im}(\mathbf{E}^* \times \mathbf{E}) \qquad (3)$$

With E_0 the electric field of the incoming light.

The spin density is a vectorial physical quantity that describes the polarization state of light in a given plane. This density can take positive or negative values corresponding to right or left elliptical polarizations. In particular, in our reference system, a positive spin density corresponds to a right-handed helicity, a negative spin density corresponds to a left-handed helicity, and a zero density corresponds to a linear polarization. In the far field, the spin density can only take values between -1 and 1, -1 being a left circular polarization and 1 a

right circular polarization (Figure 4A and B). On the other hand, in the near field, the spin density normalized to the incident intensity $|E_0|^2$ can take much larger values due to the increase of the fields, leading to the concept of super-circular light by analogy with super-chiral light.[49] Therefore, since the generation of drift currents requires an elliptical or circular polarization (Equation (1)), by creating locally non-zero spin densities, the generation of an IFE is possible in a plasmonic structure. Here, the chiral property of our optimized design comes from the fact that for excitation for two different circular polarizations, only one polarization generates locally a non-zero spin density (Figure 4C and D), the one that is right circular (Figure 4D). This behavior results from constructive and destructive interferences of the light locally around the plasmonic structure. Similarly, for the mirror plasmonic structure (Figure 4E and F), only one opposite light helicity generates a non-zero spin density, the left circular polarization (Figure 4E). Moreover, as can be seen in Figure 4D and E, the signs of the local spin densities generated in the nanostructures are opposite. It is positive in the case of a right circular excitation (Figure 4D), corresponding to a right elliptical polarization, and negative in the case of a left circular excitation (Figure 4E), corresponding to a left elliptical polarization. As a result of the IFE, the optimized structure thus generates a **B**-field oriented in the propagating wave direction and the mirror structure in the counter-propagating one. Finally, the high amplitude of the generated **B**-field is directly related to the super-circular nature of the light generated by these plasmonic structures, creating, in turn, strong drift currents.

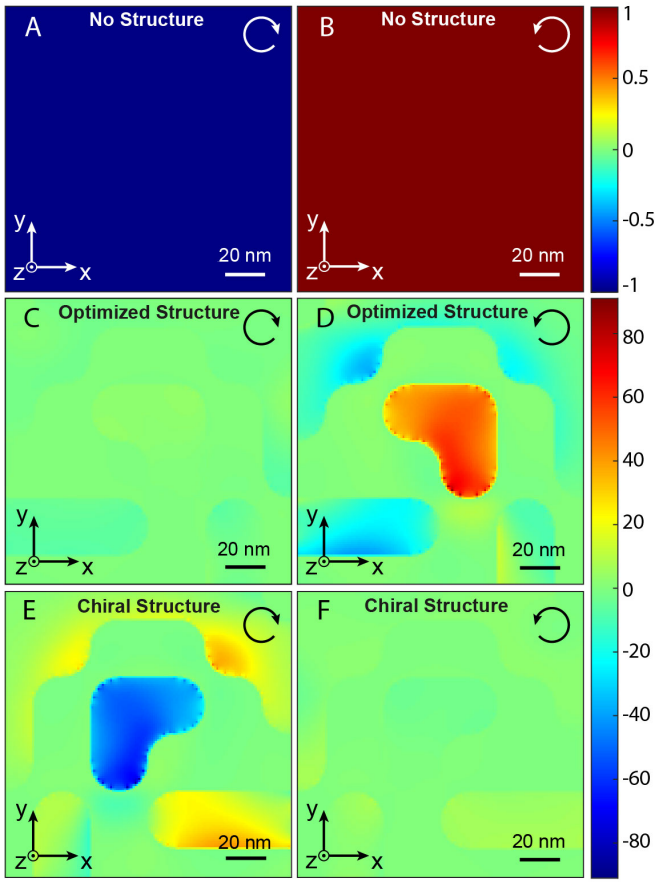

Figure 4: Distribution of spin densities. A) And B) spin density for left and right circularly polarized plane waves, respectively. C) and D) Local spin density in the Z-center of the optimized plasmonic nanostructure for left and right circular polarization of excitation, respectively. E) and F) Local spin density in the Z-center of the mirror plasmonic structure of the optimized one, for excitation by E) a left or F) right circularly polarized wave. The white and black arrows indicate the incoming polarizations.

3. Conclusion

In conclusion, we have demonstrated for the first time that the magneto-optical process of the inverse Faraday effect can be a chiral mechanism occurring only for one helicity of light. This new physical effect is due to manipulating the light polarization at the nanoscale. Using

an inverse design algorithm based on natural selection, we have shown the generation of a non-zero spin density locally in a plasmonic nanostructure for a single helicity of light, making the selective magnetization possible as a function of the excitation polarization. Also, we have demonstrated that using a mirror structure allows the generation of a **B**-field equivalent in size and amplitude but of opposite orientation, demonstrating a perfect chirality effect. Finally, due to the super-circular light created by these structures, a concept similar to super-chiral light and which describes an elliptical polarization of the light where the optical fields are strongly increased, the generated **B**-field has an amplitude of 0.5 T, which makes it one of the most intense generated at these scales and by IFE. The results presented here are significant for several reasons. The IFE by plasmonic nanostructures is the only approach allowing for the generation of ultrafast magnetic field pulses at the nanometer scale. The possibility of generating a structure-defined magnetic field for unpolarized excitation would have applications in the manipulation of magnetic processes such as skyrmion manipulation, ultrafast magnetic modulation, magnetic trapping, spin currents, or spin precession, with, for example, ultrafast data writing as a direct application.

Author contributions: All the authors have accepted responsibility for the entire content of this submitted manuscript and approved submission.

Research funding: This work is supported by the Agence National de la Recherche (ANR-20-CE09-0031-01), the Institut de Physique du CNRS (Tremplin@INP 2020) and the China Scholarship Council.

Conflict of interest statement: The authors declare no conflict of interest regarding this article.

Bibliography

[1] L. Pitaevskii, "Electric forces in a transparent dispersive medium," *Sov. Phys. JETP*, vol. 12, pp. 1008-1013, 1961.
[2] J. Van der Ziel, P. S. Pershan, and L. Malmstrom, "Optically-induced magnetization resulting from the inverse Faraday effect," *Phys. Rev. Lett.*, vol. 15, pp. 190, 1965.
[3] P. Pershan, J. Van der Ziel, and L. Malmstrom, "Theoretical discussion of the inverse Faraday effect, Raman scattering, and related phenomena," *Phys. Rev.*, vol. 143, pp. 574, 1966.
[4] J. Deschamps, M. Fitaire, and M. Lagoutte, "Inverse Faraday effect in a plasma," *Phys. Rev. Lett.*, vol. 25, pp. 1330, 1970.
[5] V. Tsytovich, "Magnetic-field generation in collisionless plasmas," *Comments on Plasma Physics and Controlled Fusion*, vol. 4, pp. 81-89, 1978.
[6] P. Mora, and R. Pellat, "Ponderomotive effects and magnetic field generation in radiation plasma interaction," *The Physics of Fluids*, vol. 22, pp. 2408-2417, 1979.
[7] R. Hertel, "Theory of the inverse Faraday effect in metals," *J. Magn. Magn. Mater.*, vol. 303, pp. L1-L4, 2006.
[8] V. Karpman, and A. Shagalov, "The ponderomotive force of a high-frequency electromagnetic field in a cold magnetized plasma," *Journal of Plasma Physics*, vol. 27, pp. 215-224, 1982.
[9] H. Hora, Laser Plasma Physics: forces and the nonlinearity principle, Spie Press (2000).
[10] R. Hertel, and M. Fähnle, "Macroscopic drift current in the inverse Faraday effect," *Phys. Rev. B*, vol. 91, pp. 020411, 2015.
[11] I. I. Smolyaninov, C. C. Davis, V. N. Smolyaninova, D. Schaefer, J. Elliott, and A. V. Zayats, "Plasmon-induced magnetization of metallic nanostructures," *Phys. Rev. B*, vol. 71, pp. 035425, 2005.
[12] A. Nadarajah, and M. T. Sheldon, "Optoelectronic phenomena in gold metal nanostructures due to the inverse Faraday effect," *Opt. Express*, vol. 25, pp. 12753-12764, 2017.
[13] J. Hurst, P. M. Oppeneer, G. Manfredi, and P.-A. Hervieux, "Magnetic moment generation in small gold nanoparticles via the plasmonic inverse Faraday effect," *Phys. Rev. B*, vol. 98, pp. 134439, 2018.
[14] O. H.-C. Cheng, D. H. Son, and M. Sheldon, "Light-induced magnetism in plasmonic gold nanoparticles," *Nat. Photonics*, vol. 14, pp. 365-368, 2020.
[15] R. Sinha-Roy, J. Hurst, G. Manfredi, and P.-A. Hervieux, "Driving orbital magnetism in metallic nanoparticles through circularly polarized light: A real-time tddft study," *ACS photonics*, vol. 7, pp. 2429-2439, 2020.
[16] X. Yang, Y. Mou, B. Gallas, A. Maitre, L. Coolen, and M. Mivelle, "Tesla-Range Femtosecond Pulses of Stationary Magnetic Field, Optically Generated at the Nanoscale in a Plasmonic Antenna," *ACS Nano*, vol. pp. 2021.
[17] O. H.-C. Cheng, B. Zhao, Z. Brawley, D. H. Son, and M. T. Sheldon, "Active Tuning of Plasmon Damping via Light Induced Magnetism," *Nano. Lett.*, vol. 22, pp. 5120-5126, 2022.
[18] D. Bossini, V. I. Belotelov, A. K. Zvezdin, A. N. Kalish, and A. V. Kimel, "Magnetoplasmonics and femtosecond optomagnetism at the nanoscale," *Acs Photonics*, vol. 3, pp. 1385-1400, 2016.
[19] E. Beaurepaire, J.-C. Merle, A. Daunois, and J.-Y. Bigot, "Ultrafast spin dynamics in ferromagnetic nickel," *Phys. Rev. Lett.*, vol. 76, pp. 4250, 1996.

[20] I. Zubritskaya, N. Maccaferri, X. Inchausti Ezeiza, P. Vavassori, and A. Dmitriev, "Magnetic control of the chiroptical plasmonic surfaces," *Nano. Lett.*, vol. 18, pp. 302-307, 2018.
[21] N. Maccaferri, I. Zubritskaya, I. Razdolski et al., "Nanoscale magnetophotonics," *J. Appl. Phys.*, vol. 127, pp. 080903, 2020.
[22] K. Mishra, A. Ciuciulkaite, M. Zapata-Herrera et al., "Ultrafast demagnetization in a ferrimagnet under electromagnetic field funneling," *Nanoscale*, vol. 13, pp. 19367-19375, 2021.
[23] G. Petrucci, A. Gabbani, I. Faniayeu et al., "Macroscopic magneto-chiroptical metasurfaces," *Appl. Phys. Lett.*, vol. 118, pp. 251108, 2021.
[24] K. Mishra, R. M. Rowan-Robinson, A. Ciuciulkaite et al., "Ultrafast Demagnetization Control in Magnetophotonic Surface Crystals," *Nano. Lett.*, vol. 22, pp. 9773-9780, 2022.
[25] A. Kirilyuk, A. V. Kimel, and T. Rasing, "Ultrafast optical manipulation of magnetic order," *Reviews of Modern Physics*, vol. 82, pp. 2731, 2010.
[26] K.-M. C. Fu, S. M. Clark, C. Santori, C. R. Stanley, M. Holland, and Y. Yamamoto, "Ultrafast control of donor-bound electron spins with single detuned optical pulses," *Nat. Phys.*, vol. 4, pp. 780-784, 2008.
[27] H.-I. Lu, I. Kozyryev, B. Hemmerling, J. Piskorski, and J. M. Doyle, "Magnetic trapping of molecules via optical loading and magnetic slowing," *Phys. Rev. Lett.*, vol. 112, pp. 113006, 2014.
[28] S.-G. Je, P. Vallobra, T. Srivastava et al., "Creation of magnetic Skyrmion bubble lattices by ultrafast laser in ultrathin films," *Nano. Lett.*, vol. 18, pp. 7362-7371, 2018.
[29] V. V. Temnov, "Ultrafast acousto-magneto-plasmonics," *Nat. Photonics*, vol. 6, pp. 728, 2012.
[30] T. Ishii, H. Yamakawa, T. Kanaki et al., "Ultrafast magnetization modulation induced by the electric field component of a terahertz pulse in a ferromagnetic-semiconductor thin film," *Scientific reports*, vol. 8, pp. 1-6, 2018.
[31] A. Khorsand, M. Savoini, A. Kirilyuk et al., "Role of magnetic circular dichroism in all-optical magnetic recording," *Phys. Rev. Lett.*, vol. 108, pp. 127205, 2012.
[32] M. Fechner, A. Sukhov, L. Chotorlishvili, C. Kenel, J. Berakdar, and N. A. Spaldin, "Magnetophononics: Ultrafast spin control through the lattice," *Physical Review Materials*, vol. 2, pp. 064401, 2018.
[33] A. Greilich, S. E. Economou, S. Spatzek et al., "Ultrafast optical rotations of electron spins in quantum dots," *Nat. Phys.*, vol. 5, pp. 262-266, 2009.
[34] A. Schellekens, K. Kuiper, R. De Wit, and B. Koopmans, "Ultrafast spin-transfer torque driven by femtosecond pulsed-laser excitation," *Nat. Commun.*, vol. 5, pp. 4333, 2014.
[35] T. Satoh, Y. Terui, R. Moriya et al., "Directional control of spin-wave emission by spatially shaped light," *Nat. Photonics*, vol. 6, pp. 662-666, 2012.
[36] J. T. Collins, C. Kuppe, D. C. Hooper, C. Sibilia, M. Centini, and V. K. Valev, "Chirality and chiroptical effects in metal nanostructures: fundamentals and current trends," *Advanced Optical Materials*, vol. 5, pp. 1700182, 2017.
[37] T. Feichtner, O. Selig, M. Kiunke, and B. Hecht, "Evolutionary optimization of optical antennas," *Phys. Rev. Lett.*, vol. 109, pp. 127701, 2012.
[38] P. R. Wiecha, A. Arbouet, C. Girard, A. Lecestre, G. Larrieu, and V. Paillard, "Evolutionary multi-objective optimization of colour pixels based on dielectric nanoantennas," *Nat. Nanotechnol.*, vol. 12, pp. 163, 2017.
[39] N. Bonod, S. Bidault, G. W. Burr, and M. Mivelle, "Evolutionary Optimization of All-Dielectric Magnetic Nanoantennas," *Advanced Optical Materials*, vol. 7, pp. 1900121, 2019.

[40] J. Krüger, D. Dufft, R. Koter, and A. Hertwig, "Femtosecond laser-induced damage of gold films," *Appl. Surf. Sci.*, vol. 253, pp. 7815-7819, 2007.
[41] P. Poole, S. Trendafilov, G. Shvets, D. Smith, and E. Chowdhury, "Femtosecond laser damage threshold of pulse compression gratings for petawatt scale laser systems," *Opt. Express*, vol. 21, pp. 26341-26351, 2013.
[42] C. Ernandes, H.-J. Lin, M. Mortier, P. Gredin, M. Mivelle, and L. Aigouy, "Exploring the magnetic and electric side of light through plasmonic nanocavities," *Nano. Lett.*, vol. 18, pp. 5098-5103, 2018.
[43] M. Sanz-Paz, C. Ernandes, J. U. Esparza et al., "Enhancing magnetic light emission with all-dielectric optical nanoantennas," *Nano. Lett.*, vol. 18, pp. 3481-3487, 2018.
[44] A. Singh, P. M. de Roque, G. Calbris, J. T. Hugall, and N. F. van Hulst, "Nanoscale mapping and control of antenna-coupling strength for bright single photon sources," *Nano. Lett.*, vol. 18, pp. 2538-2544, 2018.
[45] A. G. Curto, G. Volpe, T. H. Taminiau, M. P. Kreuzer, R. Quidant, and N. F. van Hulst, "Unidirectional emission of a quantum dot coupled to a nanoantenna," *Science*, vol. 329, pp. 930-933, 2010.
[46] J. García-Guirado, M. Svedendahl, J. Puigdollers, and R. Quidant, "Enantiomer-selective molecular sensing using racemic nanoplasmonic arrays," *Nano. Lett.*, vol. 18, pp. 6279-6285, 2018.
[47] J. Garcia-Guirado, M. Svedendahl, J. Puigdollers, and R. Quidant, "Enhanced chiral sensing with dielectric nanoresonators," *Nano. Lett.*, vol. 20, pp. 585-591, 2019.
[48] T. Hanke, G. Krauss, D. Träutlein, B. Wild, R. Bratschitsch, and A. Leitenstorfer, "Efficient nonlinear light emission of single gold optical antennas driven by few-cycle near-infrared pulses," *Phys. Rev. Lett.*, vol. 103, pp. 257404, 2009.
[49] X. Yang, Y. Mou, R. Zapata, B. Reynier, B. Gallas, and M. Mivelle, "An inverse Faraday effect generated by linearly polarized light through a plasmonic nano-antenna," *Nanophotonics*, vol. pp. 2023.

Supporting information

A Chiral Inverse Faraday Effect Mediated by an Inversely Designed Plasmonic Antenna

Ye Mou, Xingyu Yang, Bruno Gallas, and Mathieu Mivelle*

Sorbonne Université, CNRS, Institut des NanoSciences de Paris, INSP, F-75005 Paris, France

*Corresponding author: mathieu.mivelle@sorbonne-universite.fr

A list of the main content:

Simulation parameters

Supporting figures S1 to S8

Simulation parameters:

The simulations carried out in this study were done by the finite difference time domain (FDTD) method performed on the commercial software Lumerical from Ansys. This method solves Maxwell's equations in space and time using a finite difference technique. Indeed, the FDTD method solves these equations on a discrete spatial and temporal grid. The dimensions of the 3D computational window for the simulations were 750x750x900 nm^3. The boundary conditions of this window are made of a perfectly matched layer (PML), avoiding any parasitic reflection inside the calculation window. Several meshes are used for the discretization of the computational space, a coarser non-uniform mesh of 4 to 16 nm for the external unstructured parts, of the simulation, a finer mesh of 4 nm for a central nanostructured part of 288x288x36 nm^3 in X, Y, and Z, respectively containing the nanostructures, and an even finer mesh of 1 nm for the part where the drift currents and magnetic field are calculated of 140x140x32 nm^3 in X, Y, and Z (Figure S1C). The choice of this mesh size for the central part is chosen because convergence in the amplitude of the magnetic field is observed starting from this mesh size (Figure S8). The excitation of the nanostructures is performed by a pulsed plane wave of duration 5.3 fs spectrally centered at a wavelength of 800 nm. The peak power of the pulse is 10^{12} W/cm^2, which corresponds to an energy slightly lower than 4.8 pJ applied to the plasmonic nanostructures (energy density of 5.3 mJ/cm^2). The convergence of the simulation was obtained when the energy inside the calculation window was lower than 10^{-5} of the initial injected energy. The textbook values of Johnson and Christy were used for the gold properties in these simulations.

Supporting figures:

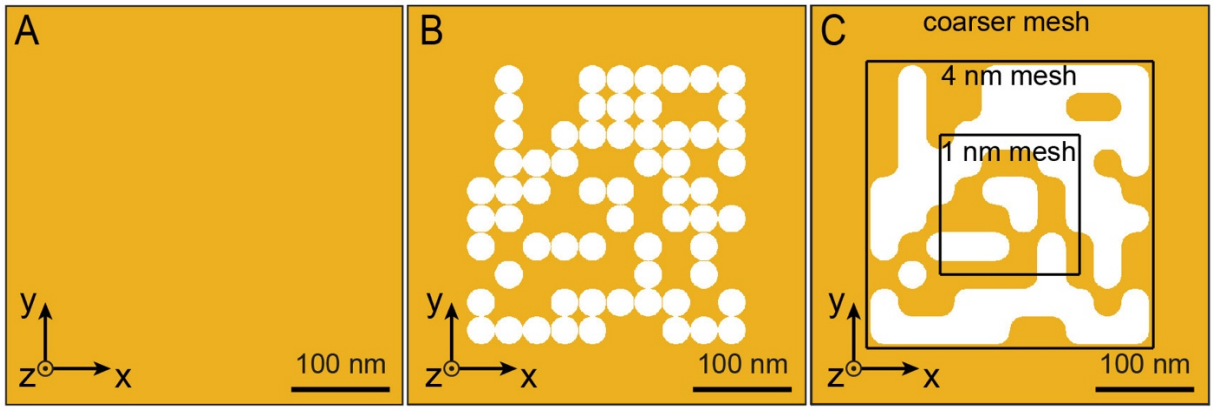

Figure S1: Construction of the elements constituting each generation of the genetic algorithm. Inside A) a uniform gold layer of 30 nm thickness, holes are made according to a binary matrix playing the role of the DNA in the evolutionary process. C) The obtained structure is then smoothed to avoid all the roughnesses not experimentally feasible and generating non-physical effects. The different mesh areas are shown in C.

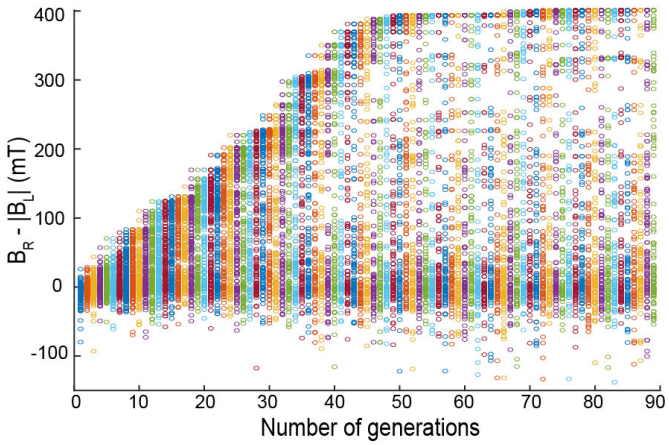

Figure S2: Evolutionary process. Evolution during the different generations of the optimization function consisting in maximizing the difference $\mathbf{B}_{RCP}$-abs($\mathbf{B}_{LCP}$), with $\mathbf{B}_{RCP}$ and $\mathbf{B}_{LCP}$ the **B**-fields created by a right or left circular polarization, respectively. Each generation consists of 200 structures. The optimized structure appears after 76 generations.

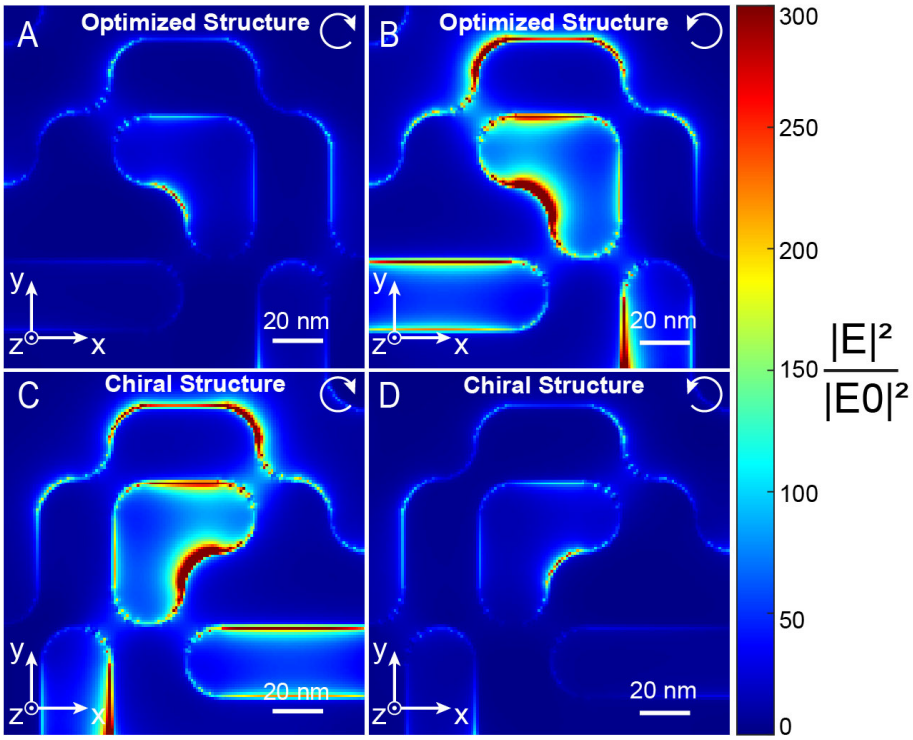

Figure S3: Optical responses in an XY plane. A) and B) Spatial distributions of the optical electric intensity enhancement at the surface of the optimized structure (2 nm below the upper edge of the gold layer) for the left and right circular polarizations of excitation, respectively. C) and D) Spatial distributions of the optical electric intensity enhancement at the surface of the mirror structure for the left and right circular polarizations of excitation, respectively. The white arrows indicate the incoming polarizations.

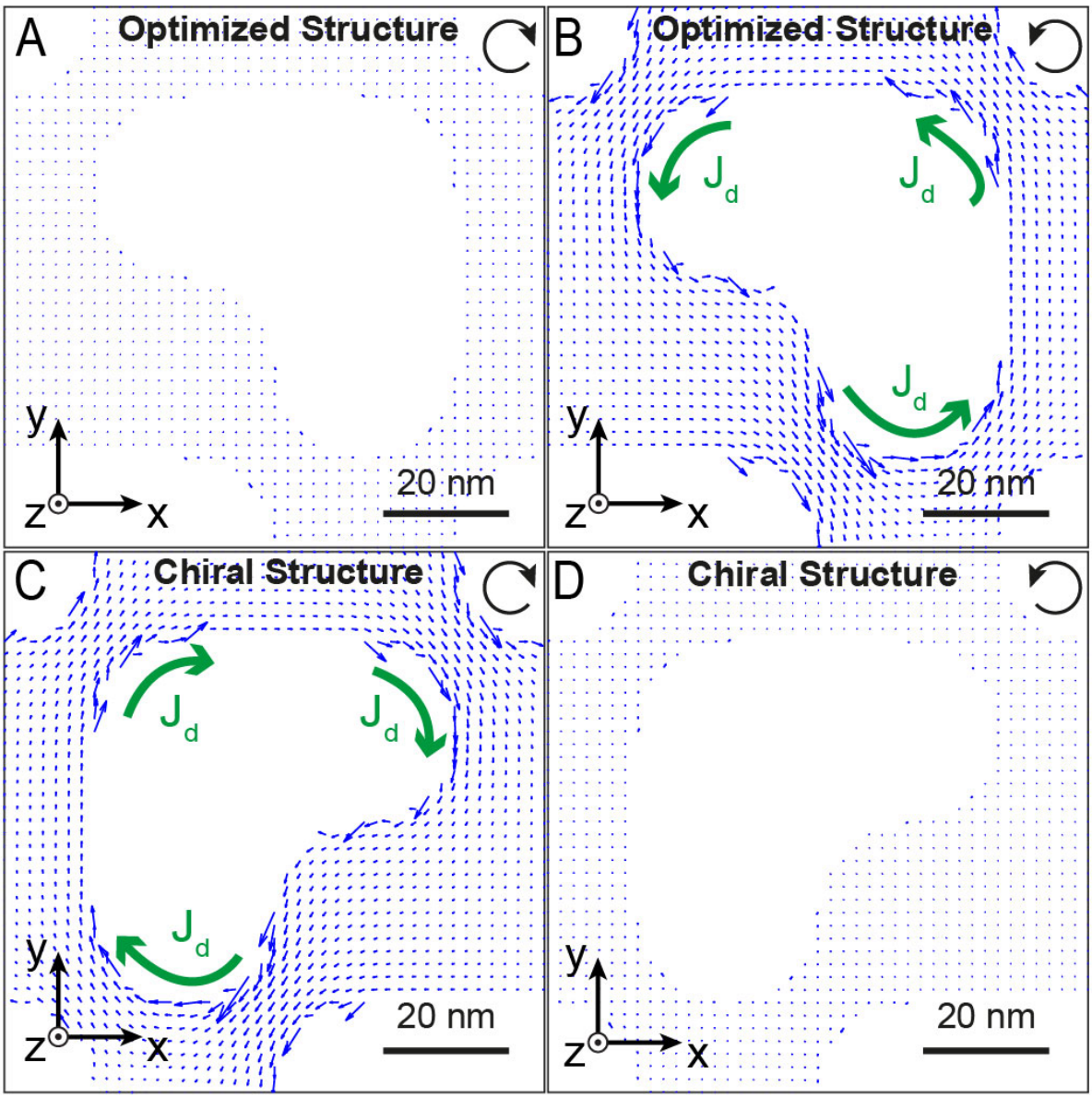

Figure S4: Distribution of drift currents in an XY plane. A) and B) Spatial distributions of drift currents at the surface (2 nm below the upper edge of the gold layer) of the optimized structure for the left and right circular polarizations of excitation, respectively. C) and D) Spatial distributions of drift currents at the surface of the mirror structure for the left and right circular polarizations of excitation, respectively. The black arrows indicate the incoming polarizations.

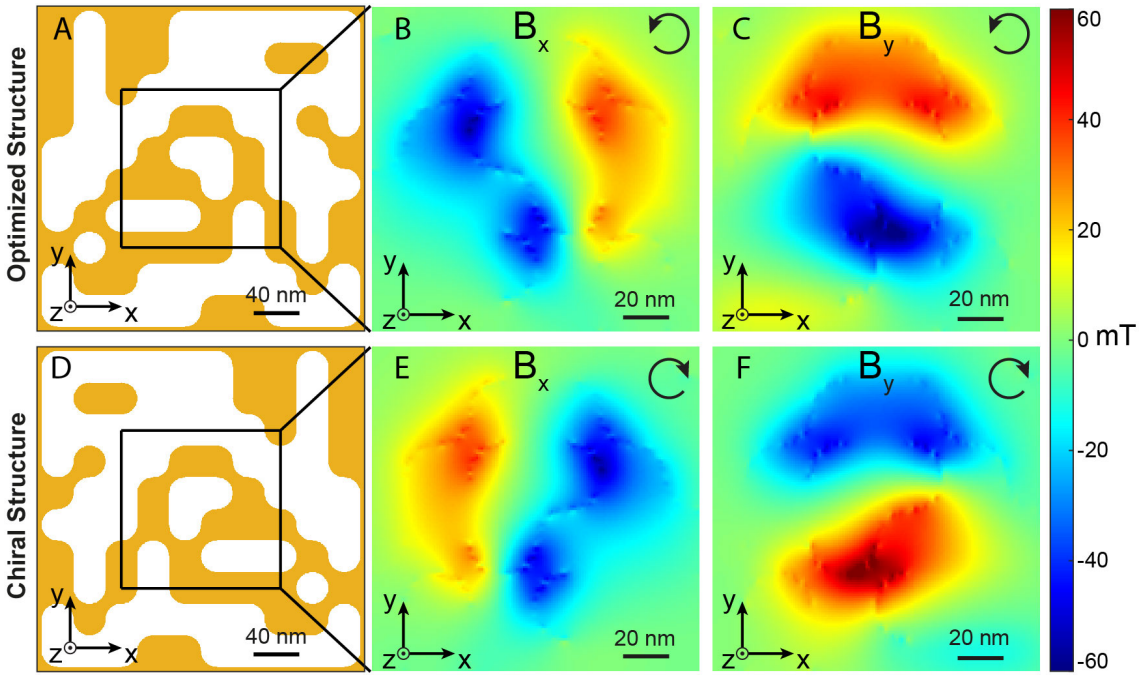

Figure S5: Vectorial magnetic field components. A) Schematic, in an XY plane, of the GA-optimized structure. B) and C) Spatial distributions of the **B**-field along X ($\mathbf{B_x}$) and the **B**-field along Y ($\mathbf{B_y}$) generated at the Z-center of the structure shown in A) for the right circular polarizations of excitation. D) Schematic, in an XY plane, of the mirror structure. E) and F) Spatial distributions of $\mathbf{B_x}$ and $\mathbf{B_y}$ generated at the Z-center of the mirror structure shown in D) for the left circular polarizations of excitation. The black arrows indicate the incoming polarizations.

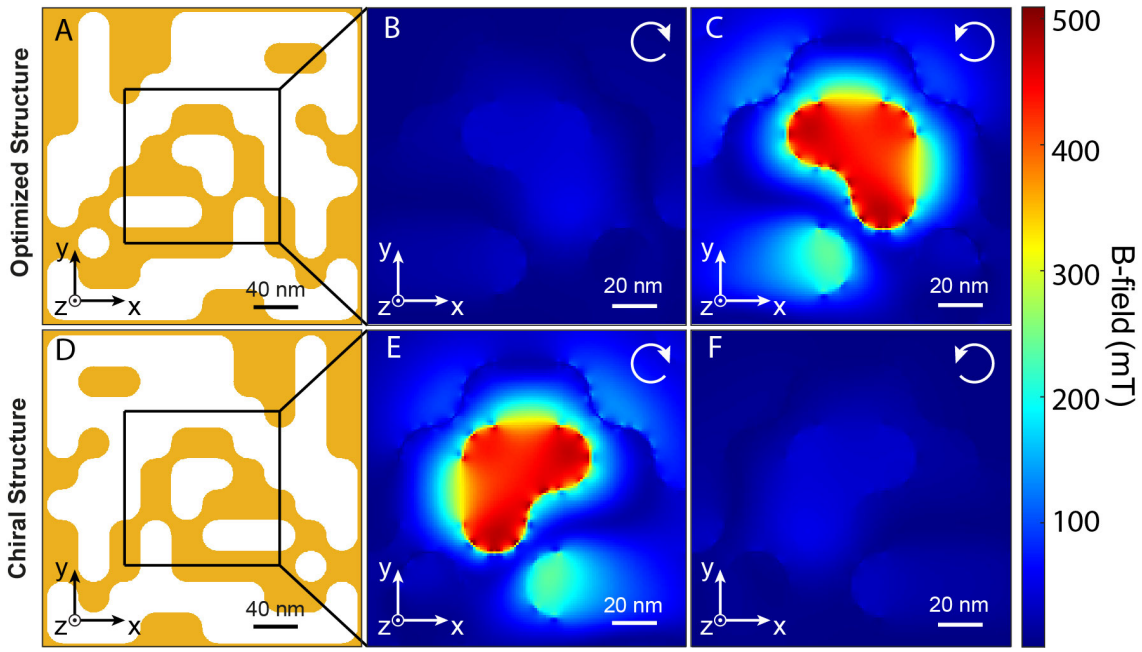

Figure S6: Amplitude of magnetic fields. A) Schematic, in an XY plane, of the GA-optimized structure. B) and C) Spatial distributions of the **B**-field amplitude at the Z-center of the structure shown in A) for the left and right circular polarizations of excitation, respectively. D) Schematic, in an XY plane, of the mirror structure. E) and F) Spatial distributions of **B**-field amplitude at the Z-center of the mirror structure shown in D) for the left and right circular polarizations of excitation, respectively.The white arrows indicate the incoming polarizations.

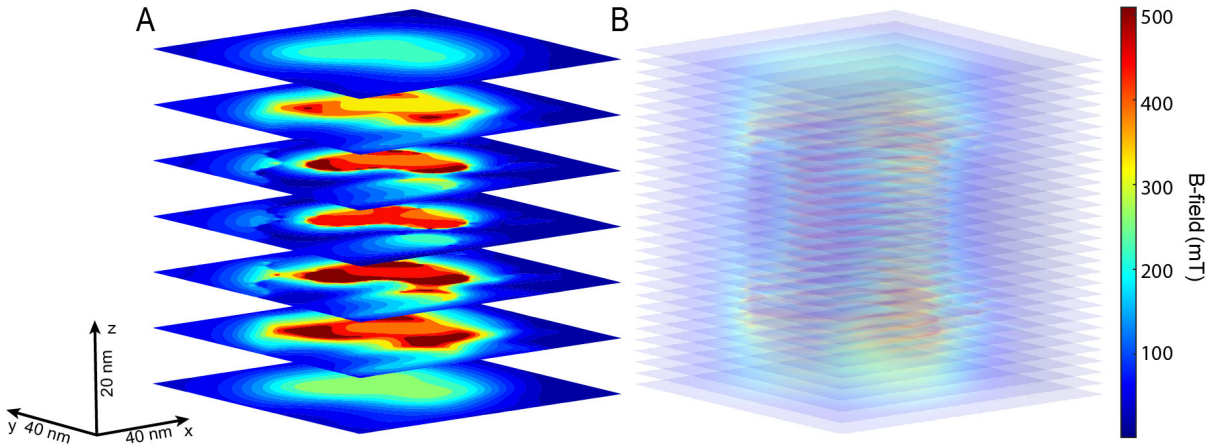

Figure S7: Amplitude of magnetic fields in 3D. XY amplitude distributions of the magnetic field B in different Z planes from -15 nm below the gold layer to +15 nm above it in steps of A) 10 nm and B) 2 nm. The distributions in figure B) are partially transparent in order to obtain a 3D representation of this magnetic field distribution.

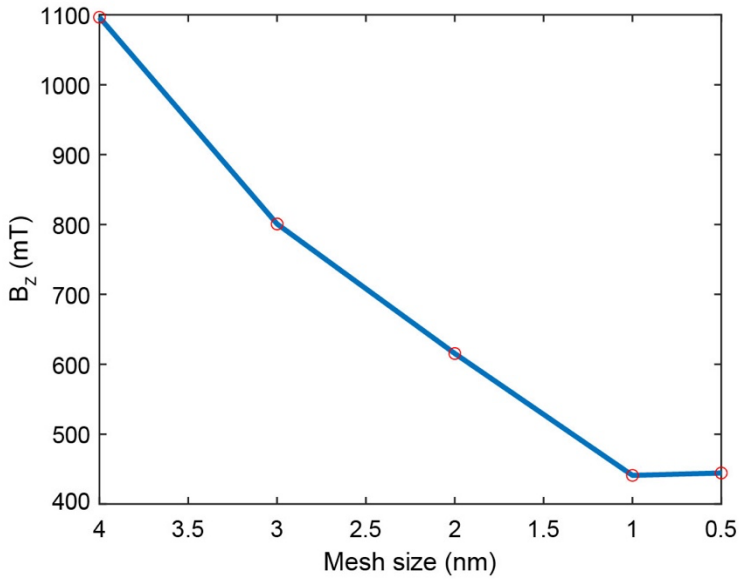

Figure S8: Amplitude of the magnetic field oriented along Z and generated by the optimized nanostructure for excitation by a right circular polarization and for different mesh sizes of the central zone. A convergence is observed from a mesh size of 1 nm, justifying the choice of the latter in the central zone of 140x140x32 nm^3